

Spectroscopy of the superconducting proximity effect in nanowires using integrated quantum dots

Christian Jünger¹, Andreas Baumgartner¹, Raphaëlle Delagrangé¹, Denis Chevallier¹, Sebastian Lehmann², Malin Nilsson², Kimberly A. Dick^{2,3}, Claes Thelander² & Christian Schönenberger¹

¹*Department of Physics, University of Basel, Klingelbergstrasse 82, CH-4056 Basel, Switzerland*

²*Division of Solid State Physics and NanoLund, Lund University, S-221 00 Lund, Sweden*

³*Center for Analysis and Synthesis Lund University, S-221 00 Lund, Sweden*

The superconducting proximity effect has been the focus of significant research efforts over many years and has recently attracted renewed interest as the basis of topologically non-trivial states in materials with a large spin orbit interaction, with protected boundary states useful for quantum information technologies. However, spectroscopy of these states is challenging because of the limited spatial and energetic control of conventional tunnel barriers. Here, we report electronic spectroscopy measurements of the proximity gap in a semiconducting indium arsenide (InAs) nanowire (NW) segment coupled to a superconductor (SC), using a spatially separated quantum dot (QD) formed deterministically during the crystal growth. We extract the characteristic parameters describing the proximity gap which is suppressed for lower electron densities and fully developed for larger ones. This gate-tunable transition of the proximity effect can be understood as a transition from the long to the short junction regime of subgap bound states in the NW segment. Our device architecture opens up the way to systematic, unambiguous spectroscopy studies of subgap bound states, such as

Majorana bound states.

Introduction

Coupling a superconductor (SC) to a metal or a semiconductor results in the so called superconducting proximity effect in the normal material¹. If the proximitised material is a low-dimensional semiconductor, this phenomenon can, for example, be used as a source of spin-entangled electrons^{2,3} or superconducting magnetometers⁴. By combining an s-wave SC with a one-dimensional semiconducting nanowire (NW) with large spin orbit interaction, one can artificially create a proximity region with superconductivity of p-wave character. This can give rise to exotic quantum states at the ends of the SC, such as Majorana bound states⁵⁻⁸, potentially useful as building blocks for topological quantum information processing^{9,10}. However, an unambiguous characterization of superconducting subgap states and the proximity region in NWs remains challenging. Several theoretical proposals suggest to use a quantum dot (QD) as a spectrometer to investigate Majorana bound state lifetime^{11,12}, spin texture¹³ or parity¹⁴. A first experiment was reported recently in which the QD was defined by electrical gating⁷. However, a systematic and deterministic spectroscopy, requires a spatially well defined, weakly coupled, QD with sharp tunnel barriers across the complete NW, which does not hybridise with the bound states or the SC under investigation. Here, we introduce a new material platform that allows us to perform ideal tunnel spectroscopy: we use an in-situ grown axial QD in an InAs NW covering the complete diameter of the NW, to probe the superconducting proximity region of a NW segment close to the superconducting contact. The

QD is defined by two potential barriers that form when the NW crystal structure is changed from zincblende (ZB) to wurtzite (WZ), which can be achieved with atomic precision by controlling the growth parameters^{15,16}. These QDs are electrically and spatially well defined, which allows us to probe the induced gap at a precise distance from the QD and with predictable coupling parameters. In-situ grown barriers have previously been used to investigate double QD physics^{17,18}. Here, we use such artificial QDs to study the evolution of the proximity induced superconductivity in a controlled and systematic manner. We demonstrate this type of spectroscopy using two different transport regimes of the QD: in the cotunneling regime, where the QD can be seen as a single tunnel barrier, and in the sequential tunneling regime, where the QD acts as an energy filter with Coulomb blockade (CB) resonances. The complementary measurements allow us to draw a clear picture of how the proximity gap forms in a NW segment, for which we present an intuitive explanation supported by numerical simulations.

Results

Device and characterization. We use an InAs NW with an in situ grown axial QD formed by controlling its crystal phase structure in the growth direction¹⁶: two thin segments (30 nm) of WZ phase are grown in the otherwise ZB NW. These segments act as atomically precise hard-wall tunnel barriers for electrons, because the ZB and WZ bandstructure align with a conduction band offset of ~ 100 meV^{19,20}. Consequently, in the ZB section (20 nm) between the two barriers a QD is formed¹⁹. A false color scanning electron micrograph of the actual device is shown in Fig.1a, together with a transmission electron micrograph of the atomically precise interface in a represen-

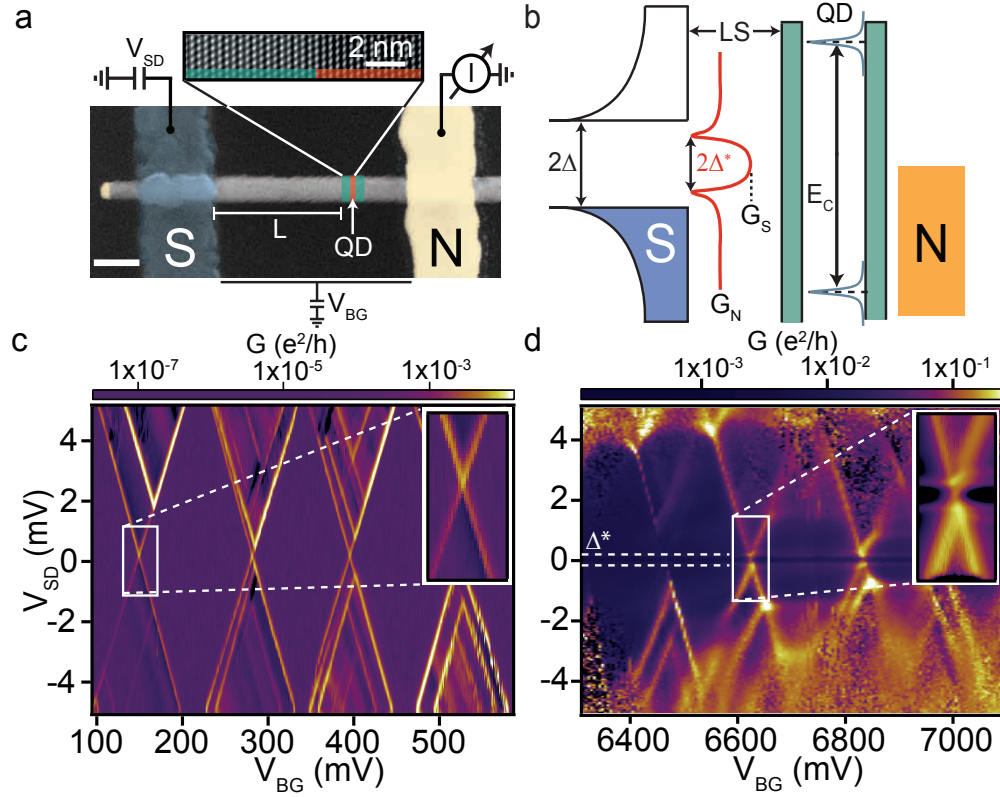


Figure 1: Crystal phase engineered QD in an S - N - QD device. **a** False color scanning electron micrograph of the investigated device, consisting of a superconductor S (blue) - InAs NW - normal metal N (yellow) junction (scale bar: 100 nm). A QD (red) forms between two in-situ grown tunnel barriers (green) in the WZ phase. The measurement scheme is shown schematically. The inset shows a high resolution transmission electron micrograph of the atomically sharp ZB/WZ interface of a comparable NW. **b** Energy diagram of such a system with an illustration of the proximity gap Δ^* in the lead segment (LS). **c** Differential conductance G as a function of the backgate voltage V_{BG} and the source-drain bias V_{SD} in the superconducting state. The inset shows a single CB resonance in more detail. **d** CB diamonds at higher backgate voltages exhibiting a gap in the transport characteristics.

tative NW in the inset. The superconducting electrode consists of titanium/aluminum (Ti/Al) and the normal contact of titanium/gold (Ti/Au), fabricated by electron beam lithography. The differential conductance $G = dI/dV_{SD}$ as a function of the backgate voltage V_{BG} in the normal state (in an external magnetic field of $B = 50$ mT) shows regularly spaced CB resonances (see supplementary material Fig.S1a) for which we find a systematic increase of the total tunnel coupling Γ with increasing V_{BG} (see Fig.S1b), consistent with the lowering of the tunnel barrier when the bandstructure is shifted to lower energies with respect to the Fermi energy (see schematic in Fig.S2)¹⁹. In the device discussed here, the QD is located about $L \approx 350$ nm from the Al electrode, leaving a bare NW segment of this length between the QD and the SC, which we refer to as the “lead segment” (LS). This provides a new experimental situation, as the QD is not directly coupled to the SC (as it might be the case in other experiments^{21–23}) and can be used to probe the LS. V_{BG} here directly tunes the chemical potential in both the LS and the QD. We record G as a function of the bias voltage V_{SD} applied between the SC and the normal metal contact. If the electrons would tunnel directly from the QD to the superconducting electrode, we would expect to see a gap similar to the one of the bulk $\Delta \approx 210 \mu\text{eV}$ ²⁴ of the SC, independent of V_{BG} . Since most of the bias drops over the QD, G is proportional to the density of states (DOS) in the LS. This is the case for positive V_{BG} where carriers accumulate in the NW. Therefore we can perform spectroscopy on the LS by tunneling from the QD (see Fig.1b).

An interesting transition in the conductance can already be found in the overview data in Fig.1c,d presenting regular CB diamonds in the superconducting state (charging energy $E_c \approx 6$ meV, level spacing $\epsilon \approx 1.5$ meV to 2 meV) for two different regimes of V_{BG} . While for positive gate voltages

$V_{BG} \gtrsim 3 \text{ V}$ we observe a superconducting gap around zero bias (c.f. Fig.1d), for low gate voltages (c.f. Fig.1c) we do not find any features related to superconductivity, but rather the standard sequence of diamonds.

Measurements. The QD can be used as a spectrometer in two different regimes. In the first regime, the QD is kept deep in the CB regime where the charge is fixed for bias voltages in the range of the proximity induced gap Δ^* , since $\Delta^* \ll E_c$. In this regime transport is mediated by cotunneling, which is a second order process involving the virtual occupation of a QD state²⁵. Here, the QD can be thought of as a single tunnel barrier. In the second regime, the QD electrochemical potential is tuned to to a CB resonance, with transport occurring as first order sequential tunneling. In the following, we discuss the experiments in the two regimes one after the other.

First, we investigate the cotunneling regime, where we can understand the SC - LS as an S-N junction which is weakly coupled to the QD. The measured spectrum is shown in Fig.S3a. It can be characterized by four quantities: the magnitude of the observed gap Δ^* , the full width at half the maximum (FWHM) of the peaks at the gap edge, the normal state conductance G_N measured at a bias $|V_{SD}| > \Delta^*/e$ and G_S the conductance at $V_{SD} = 0$. Since the conductance is not fully suppressed at zero bias, we characterise this softness by defining the suppression factor $S = G_S/G_N$. Figures 2a-c show G as a function of V_{BG} and V_{SD} for three different backgate regimes. Cross sections (Fig.2c: averaged over 20 cross sections in the CB diamond centers) at different V_{BG} in the CB regime are plotted as blue lines. At large gate voltages ($V_{BG} \approx 7 \text{ V}$, Fig.2a) we find a clear gap around zero bias, that can be detected down to $V_{BG} \approx 2.6 \text{ V}$ (Fig.2b). The same cross sections normalized to G_N are shown in the supplementary section, Fig.S3a. All cross sections exhibit a

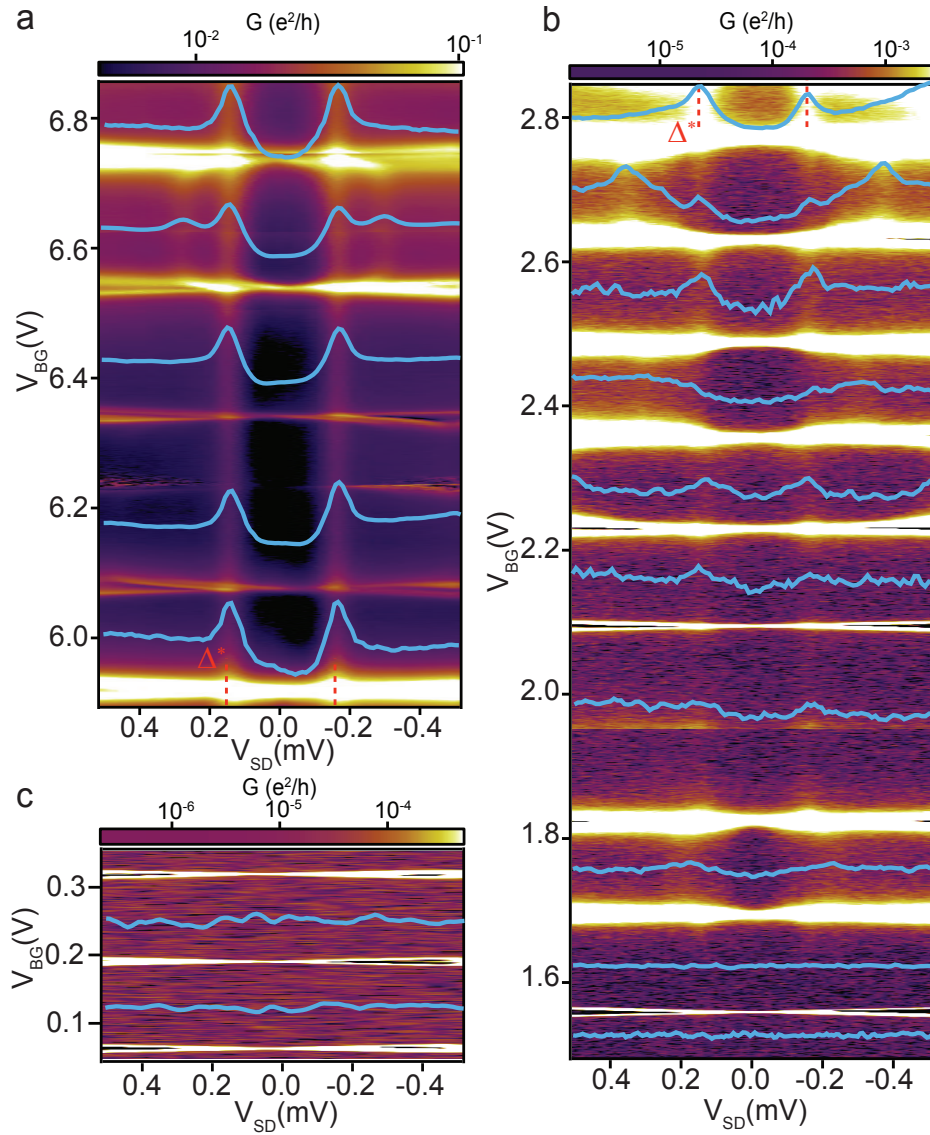


Figure 2: Proximity gap probed by cotunneling spectroscopy. Differential conductance G as a function of V_{BG} and V_{SD} for **a** high, **b** middle and **c** low backgate voltages V_{BG} . Blue lines are averaged over 20 cross sections taken in the center of the CB diamonds. The cross sections shown in **c** are averaged over the CB region between the Coulomb resonances.

suppression of G at $V_{SD} = 0$ and $\Delta^* \approx 150 \mu\text{eV}$ (position of the peak maxima). The FWHM and S are shown to be roughly constant over the investigated gate range, see Fig.S3b, with $FWHM \approx 65 \mu\text{eV} \pm 10 \mu\text{eV}$ and $S \approx 0.5 \pm 0.1$, respectively. In an ideal SC and weak coupling, S should be close to zero for a strong tunnel barrier. Larger values are often observed for proximity induced gaps, referred to as soft gap²⁶⁻²⁸. For lower gate voltages $V_{BG} < 2.6 \text{ V}$ (Fig.2b) it is difficult to perform this analysis because the cotunneling signal is very low, compared to the noise floor of the experiment ($G \approx 10^{-5} e^2/h$). However, we can still observe broad peaks down to $V_{BG} \approx 1.8 \text{ V}$. For $V_{BG} < 1.8 \text{ V}$ the differential conductance is too low to observe any signatures of superconductivity with the resolution of our measurement. For even lower gate voltages $V_{BG} \approx 0.2 \text{ V}$ (Fig. 2c) no features inside the CB diamonds can be resolved anymore. In summary, in the regime accessible by the cotunneling experiments, the proximity gap characteristics are roughly independent of the gate voltage.

To extract characteristics of the LS for a larger gate range than in the cotunneling regime, we now use the QD resonances (first order process through the QD). The left figure (“Exp.”) of each panel in Fig. 3a-d shows detailed measurements of a CB resonance in different backgate regimes, while the central panel shows a simulated map discussed below, and the right panel shows a cross section at V_{BG} as indicated in the left and central panels. In a S-QD-N system, the Coulomb diamond pattern is expected to be affected by superconductivity in the way represented in Fig. 3e. The tips of the Coulomb diamonds are expected to be shifted by $2\Delta^*/e$ in bias and by $\Delta V_{BG} = 2\Delta^*/\beta e$ (with β the lever arm of the QD) in gate voltage^{22,29}.

From the QD characteristics in the normal state (see Fig. S1a), we find that the tunnel coupling Γ

increases significantly for $V_{BG} > 2.5$ V. For large Γ , e.g. at $V_{BG} \approx 6.6$ V, a CB pattern is shown in Fig.3a. The CB resonances are broad, but clearly show a suppressed conductance around zero bias. We find a gap of $\Delta^* \approx 150 \mu\text{eV}$, confirming the value obtained in the cotunneling regime (Fig. 2).

A CB resonance with a smaller Γ value at $V_{BG} \approx 2.1$ V is shown in Fig. 3b, which is similar to the one in Fig. 3a, but with an additional resolved resonance. As expected (see Fig. 3e), the "CB diamond tips" are shifted in energy by $\pm\Delta^*/e$ and ΔV_{BG} in gate voltage, yielding a consistent value of $\Delta^* \sim 150 \mu\text{eV}$. We observe an additional resonance that crosses through the gap (white arrows). This line corresponds to the alignment of the Fermi level of the two reservoirs with the QD state. We attribute this to the tunneling through the non-zero DOS remaining at zero bias (see position I in Fig. 3e).

At $V_{BG} \approx 0.2$ V the conductance suppression is significantly reduced, as shown in Fig.3c. The CB diamond tips appear to be only slightly separated and shifted. We note that in this gate range we cannot resolve any signal in the cotunneling spectrum, as discussed in Fig. 2.

At even lower gate voltages, e.g. $V_{BG} \approx 80$ mV (Fig. 3d), we do not observe any influence of the superconducting contact, but a regular CB resonance, as found in the normal state.

To extract the characteristic numbers from these data, we use a resonant tunneling model for a S - QD - N junction. The current is then given by^{22,30} $I = \int_{-\infty}^{\infty} dE D_N(E) \cdot D_S(E + eV_{SD}) \cdot T_{QD}(E, V_{BG}, V_{SD}) \cdot [f_N(E) - f_S(E + eV_{SD})]$, with $D_N(E)$ the constant DOS of the normal metal, $T_{QD}(E, V_{BG}, V_{SD})$ a Lorentzian transmission function, accounting for the resonant tunneling through the QD and including a broadening due to the finite coupling to the electrodes.

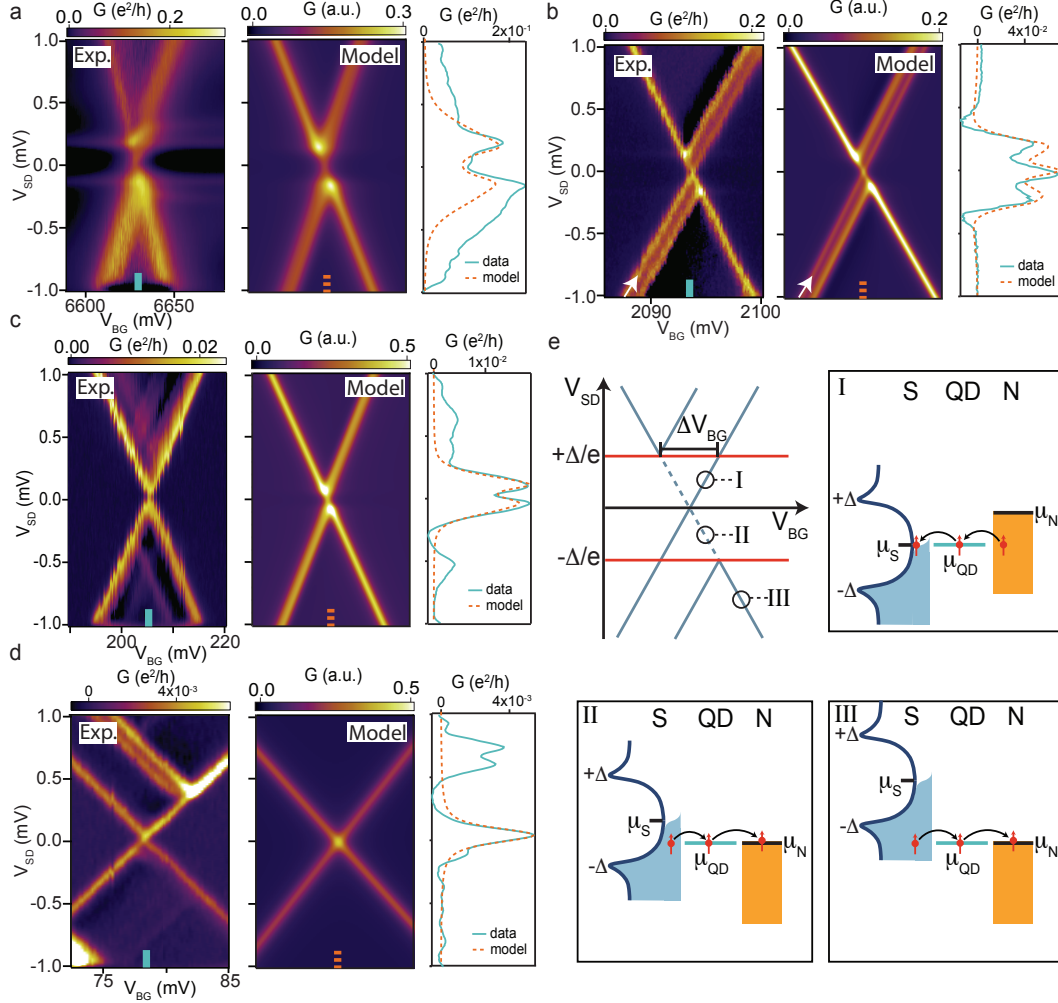


Figure 3: Proximity gap in the resonant tunneling regime. **a-d** Experiment (left) and resonant tunneling model (middle) and cross sections of both (right) for different CB resonances. Light blue and orange lines indicate the backgate voltage for the cross sections. **e** Relative positions of the electrochemical potentials of the normal contact (μ_N), the SC ($\mu_S = \mu_N - eV_{SD}$) and the QD (μ_{QD}) for selected points in a charge stability diagram. The tips of the diamonds are shifted in gate voltage by $\Delta V_{BG} = 2\Delta^*/(\beta e)$ with β the lever arm of the CB resonance. In **a** the tunnel coupling is almost a factor of 3 larger than in **b-d**. In the model, the tunnel coupling Γ is essentially constant for **b-d**, while the value for the induced superconducting energy gap varies from $\Delta^* = 165 \mu\text{eV}$ in **a**, $\Delta^* = 145 \mu\text{eV}$ in **b**, $\Delta^* = 85 \mu\text{eV}$ in **c** and $\Delta^* < 10 \mu\text{eV}$ in **d**.

$f_{S/N}$ are the Fermi distribution functions for the respective contacts. To account for the softness of the gap, the DOS in the LS can be expressed using the phenomenological Dynes parameter δ by $D_S = |\Re\epsilon(E - i\delta/\sqrt{(E - i\delta)^2 - \Delta^{*2}})|^{31}$. By adjusting the magnitude of the gap Δ^* , the QD resonance broadening Γ and the Dynes parameter δ , we get the conductance maps represented in the central panels in Fig.3a-d (“model”).

We can reproduce the characteristics of the CB resonance in Fig. 3a using $\Gamma = 150 \mu\text{eV}$, which is slightly smaller than what we obtained in the normal state. For the size of the gap we find $\Delta^* \approx 165 \mu\text{eV}$, and $\delta = 0.4 \cdot \Delta^*$ ($\delta = 65 \mu\text{eV}$), resulting in a suppression of $S \approx 0.5$, similar to what is found in the cotunneling regime. To reproduce the data in Fig. 3b we use $\Gamma = 40 \mu\text{eV}$ (similar to the numbers in the normal state), $\Delta^* \approx 145 \mu\text{eV}$ and $\delta = 0.4 \cdot \Delta^*$ ($\delta \approx 60 \mu\text{eV}$), i.e. the parameters are almost identical to the ones we obtained in the cotunneling regime at higher gate voltages. The corresponding cross sections agree well with the experiment. We note, that the conductance enhancement at the gap edge, as well as the negative differential conductance are reproduced by the model. We point out that in the sequential tunneling regime, we can extract gap characteristics down to back-gate voltages of 0.2V, which is not possible in the cotunneling regime.

To reproduce the characteristics of the CB resonance in Fig. 3c ($V_{BG} \approx 200 \text{ mV}$), we find that the tunnel coupling is similar to the one in Fig. 3b ($\Gamma = 60 \mu\text{eV}$), and $\delta = 0.5 \cdot \Delta^*$ ($\delta \approx 40 \mu\text{eV}$). However, the size of the superconducting energy gap is found to be $\Delta^* \approx 85 \mu\text{eV}$, which is significantly smaller than that found at larger gate voltages. Also here, the model reproduces the data well, illustrated in the corresponding cross sections.

Using the resonant tunneling model to simulate the resonance around $V_{BG} \approx 80 \text{ mV}$ (Fig. 3d)

we extract $\Gamma = 50 \mu\text{eV}$ and an upper limit for Δ^* of $10 \mu\text{eV}$. The model reproduces very well the characteristics of the CB resonance, which essentially corresponds to an N - QD - N device. The resonances in the experiment at higher bias outside the CB are due to excited states, which are not included in the model.

To summarize the measurements in the CB resonance regime (Fig.3): we observe a transition from a region where the LS acts as a superconducting lead (large gate voltages) with $\Delta^* \approx 165 \mu\text{eV}$ to $150 \mu\text{eV}$ to an intermediate regime with a reduced $\Delta^* \approx 85 \mu\text{eV}$, to a regime without effects of superconductivity. The parameters extracted from the resonant tunneling model demonstrate a clear evolution of Δ^* in the LS.

Discussion This evolution of the induced gap Δ^* as a function of V_{BG} is summarised on Fig. 4a. The curve shows a sharp transition from a clearly resolved energy gap for $V_{BG} > 0$ to a fully suppressed gap at $V_{BG} < 0$.

While the observed proximity feature can well be fitted with a broadened BCS DOS, this approach is not an adequate description, since there are only few states in the quasi one-dimensional NW lead. Qualitatively, one can understand the transition by considering only a few modes in the LS. All electrons at energies within the gap of the SC are Andreev reflected (AR) at the SC, giving rise to Andreev-bound states (ABSs).

We interpret the observed transition in Δ^* qualitatively as a gate-tunable transition of ABSs forming in the LS from the long to the short junction limit. Both limits are defined by comparing the physical length of the junction, L , to the characteristic length-scale $L_c = \hbar v_F / \tilde{\Delta}$, which is the coherence length in the ballistic limit³². Here v_F is the Fermi velocity in the LS, \hbar the Planck

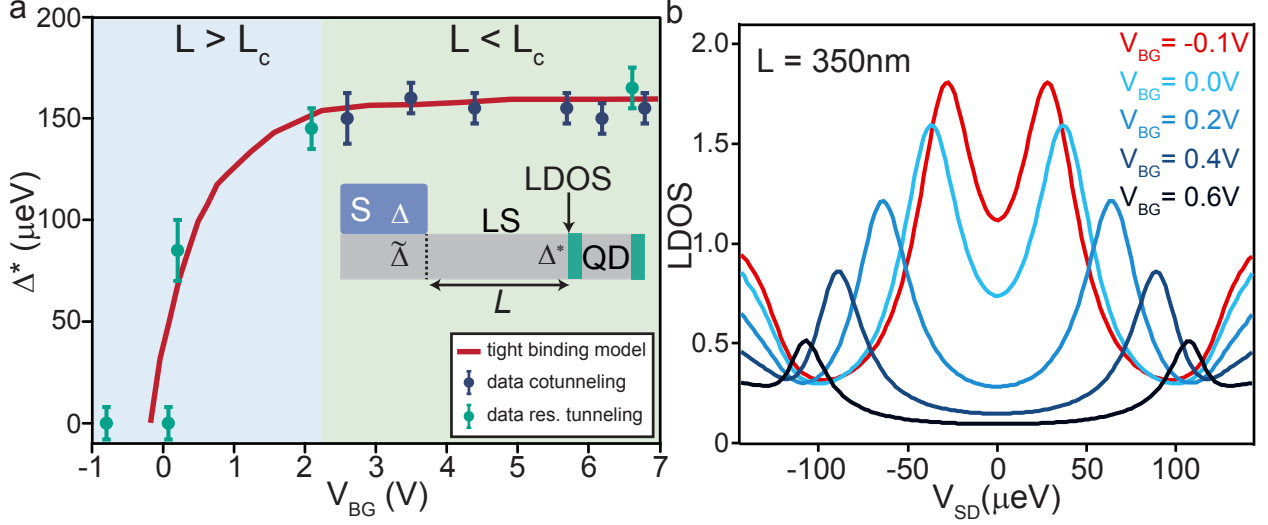


Figure 4: **a** Proximity gap Δ^* as a function of the gate voltage V_{BG} . The inset shows a schematic of the device with the relevant parameters. **b** Calculated local DOS as a function of energy for various gate voltages at a fixed distance from the interface, $L = 350$ nm.

constant and $\tilde{\Delta}$ the proximity gap induced by the aluminium contact in the NW directly below the SC (see inset of Fig. 4a).

In the short junction limit ($L \ll L_c$) the energy of the ABSs (E_{ABS}) in the LS is dominated by the phase change due to AR at the SC/LS interface (dashed line in schematic), where $\tilde{\Delta}$ is assumed to change abruptly. In this limit, the energies of the ABSs are “pushed” to $E_{ABS} \cong \tilde{\Delta}$, resulting in the superconducting proximity gap in the LS that is similar to $\tilde{\Delta}$, i.e. $\Delta^* \sim \tilde{\Delta}$ ³³. In the long junction limit ($L \gg L_c$), E_{ABS} is determined by the phase acquired in the LS, which scales with $k_f = m^* \cdot v_F / \hbar \propto v_F$, with m^* the effective electron mass. In this limit, E_{ABS} can take on smaller values, thus filling the proximity gap³². We therefore can tune E_{ABS} by tuning v_F and the electron density in the LS using V_{BG} . For very positive gate voltages, E_F is relatively far up in the con-

duction band with a correspondingly large v_F , resulting in a large L_c , bringing the LS to the short junction limit, $L < L_c$. In contrast, when we tune E_F to the bottom of the conduction band by lowering V_{BG} , v_F and L_c are strongly reduced, bringing the LS to the long junction limit, $L > L_c$, and $E_{ABS} < \tilde{\Delta}$. As a result, the apparent gap Δ^* is reduced by the ABSs moving into the gap. We note that $\tilde{\Delta}$ in the NW segment located below the SC is screened by the SC and is therefore not gate tunable.

To support this qualitative picture, we employ a numerical model, in which we combine the Green's function method with a tight binding model. The properties of the superconductor are taken into account as a self energy dressing the bare Green's function in a NW section below S , where a superconducting gap $\tilde{\Delta}$ is induced depending only on the coupling to S (details can be found in the supplementary materials). This region is coupled to a bare NW segment (of length $L = 350$ nm) modelling the LS (see inset of Fig. 4a). We then investigate the local density of states (LDOS) at a distance $L = 350$ nm as a function of the gate voltage in the NW (Fig. 4b). Like for the experimental data, we extract Δ^* as the distance between the maxima in the DOS. Here the number of ABSs as well as the ABS energy is determined by the total length of the LS. The resulting Δ^* of this calculation is plotted as a function of V_{BG} as a red line in Fig. 4a. In excellent agreement with the experiment, we observe a sharp transition in the detected gap, corresponding to the transition from the short to the long junction limit. In the model, Δ^* tends to zero when E_F is aligned with the bottom of the conduction band ($V_{BG} \approx -0.2$ V), just before the LS is fully depleted and $v_F \rightarrow 0$. For a better understanding we study the dependence of an individual ABS as a function of V_{BG} in the supplementary (see Fig. S4). Evolving from the long to the short junction limit, the states with

energy $E < \Delta^*$ move towards the gap, resulting in a fully formed smooth proximitised gap Δ^* . We note that in this model the width of the ABS is a free parameter, which we set to $25 \mu\text{eV}$. In seeming contradiction to the depleted LS, the experiment still shows several CB resonances below this gate voltage, which we attribute to evanescent modes from the NW segment below S (which is not depleted) that couples weakly to the QD wavefunctions, yielding the QD couplings highly asymmetric with very low transmission amplitudes, as observed in the experiment.

The gap in our devices is soft, i.e. the conductance suppression at zero bias is significantly lower than in NWs with an epitaxial Al shell^{34,35}. The reason for this fact remains unclear and is a priori not expected from the model. The evaporated bulk Al shows a hard gap ($S \approx 0.01$) when used in standard, large-area metallic S - I - S tunnel junctions measured in a similar experimental setup (see Fig.S5). Introducing random spatial potential fluctuations at the NW-S interface^{36,37} in the presented numerical model does not account for the observed small suppression, either (see Fig.S6). In the ABS picture, the softness of the gap is determined by the life time of the Andreev bound states in the LS. This broadening can have different physical origins, namely 1) tunneling to the QD, which should exhibit a similar tunability as the QD life time, 2) single particle tunneling to the NW segment below S, for example by an inverse proximity effect due to the gold nanoparticle used for the NW growth, and 3) quasiparticle excitation by microwave radiation absorption that might be different in NW devices compared to metallic ones.

In conclusion, we present a systematic study of the apparent transport gap in a NW segment induced by a proximity coupled superconductor. For this purpose we introduce QD tunnel spectroscopy enabled by in-situ grown axial tunnel barriers. We observe a gate-tunable transition of

the gap amplitude from a fully developed, constant proximity gap at large electron densities to smaller values and ultimately a complete suppression of the gap at low densities. The data are consistent with a transition from the short junction limit of an S-N device to the long junction limit with ABSs forming at energies also below the gap energy. This transition occurs when the Fermi energy is close to the bottom of the conduction band and the respective Fermi velocity tends towards zero. Our experiments demonstrate that NWs with in-situ grown barriers, in our example with crystal phase engineered barriers, are very useful to perform unambiguous transport spectroscopy in superconductor-semiconductor hybrid systems. We have thus introduced a novel spectroscopy tool, which is well suited to study superconducting bound states in semiconducting NWs, and open, for example, an unambiguous path for battling fundamental limitations found in recent studies of Majorana bound states^{38,39}.

Methods

Fabrication

The InAs nanowires were grown by metal-organic-vapor-phase epitaxy (MOVPE) and have an average diameter of 70 nm. The two segments of wurtzite crystal phase forming the tunnel barriers have a thickness of 30 nm. The zinc-blend segment in between, which defines the QD, has a width of 25 nm.

The nanowires were transferred mechanically from the growth substrate to a degenerately p-doped silicon substrate with a SiO₂ capping layer (400 nm). The substrate is used as a global back gate. For the electron beam lithography we employ pre-defined markers and contact pads, made of Ti/Au (5 nm/45 nm). The normal metal contact to the NW is made of Ti/Au (5 nm/70 nm) and the superconducting contact of Ti/Al (5 nm/80 nm). Before each evaporation step, the native oxide of the NW is removed by an Argon ion sputtering.

All measurements were carried out in a dilution refrigerator at a base temperature of 20 mK. Differential conductance has been measured using standard lock-in techniques ($V_{ac} = 10 \mu\text{V}$, $f_{ac} = 278 \text{ Hz}$).

Acknowledgements This work has received funding from the Swiss National Science Foundation, the Swiss Nanoscience Institute and the Swiss NCCR QSIT. C.S. has received funding from the European Research Council (ERC) under the European Unions Horizon 2020 research and innovation program: grant agreement 787414, ERC-Adv TopSupra. D.C. received funding from the European Unions Horizon 2020 research and innovation program (ERC Starting Grant, agreement No 757725). S.L., M.N., K.A.D. and C. T. acknowledge financial support by the Knut and Alice Wallenberg Foundation (KAW) and the Swedish

Research Council (VR). The authors thank C. Reeg and S. Hoffman for fruitful discussions.

Competing Interests The authors declare that they have no competing financial interests.

Author contributions C.J. fabricated the devices and performed the measurements together with R.D.. C.J., R.D. and A.B. analysed the data. A.B. provided the resonant tunneling model. D.C. provided the numerical calculations. S.L., M.N., K.A.D. and C.T. developed the nanowire structure. C.S. and A.B. planned and designed the experiments and participated in all discussions. All authors contributed to the manuscript.

Correspondence Correspondence and requests for materials should be addressed to C.J. (email: christian.juenger@unibas.ch) or A.B. (email: andreas.baumgartner@unibas.ch).

Supplementary Information

Numerical Model of a proximitised NW

We model a 1D NW with strong spin-orbit coupling partially covered by a superconductor. The total Hamiltonian for such a system can be written as $H = H_{NW} + H_S + H_T$. In the Nambu basis the creation operator of the NW electrons is given by $\hat{c}^\dagger = (c_\uparrow^\dagger, c_\downarrow^\dagger, c_\downarrow, -c_\uparrow)$, where the semiconducting nanowire Hamiltonian is

$$H_{NW} = \int \hat{c}^\dagger \left[\left(\frac{p^2}{2m} - \mu \right) \tau_z + \alpha p \sigma_y \tau_z \right] \hat{c} dx, \quad (1)$$

with $\sigma(\tau)$ the Pauli matrices in the spin (particle-hole), μ the electrochemical potential and α the strength of the Rashba spin-orbit coupling. To be able to study the gate dependence/length

dependence in our system, the Hamiltonian of the NW is described by a lattice tight-binding model where the continuum limit Hamiltonian becomes

$$H_{NW} = \sum_j^N c_j^\dagger [(t - \mu)\tau_z] c_j - \frac{1}{2} c_j^\dagger [t\tau_z + i\alpha\sigma_y\tau_z + h.c.] c_{j+1}, \quad (2)$$

with c_j^\dagger is the creation operator of an electron in the nanowire on site j written in the Nambu basis.

The Hamiltonian of the bulk superconductor can be written as

$$H_S = \sum_{\mathbf{k}, \sigma} \xi_k \Psi_{\mathbf{k}, \sigma}^\dagger \Psi_{\mathbf{k}, \sigma} + \Delta \Psi_{\mathbf{k}, \uparrow}^\dagger \Psi_{-\mathbf{k}, \downarrow}^\dagger + h.c. \quad (3)$$

with $\xi_k = \frac{k^2}{2m} - \mu$ and $\Psi_{\mathbf{k}, \sigma}$ the annihilation operator for an electron in the superconductor with spin σ and momentum \mathbf{k} . The tunneling Hamiltonian describing the coupling between the bulk SC and the nanowire takes on the form

$$H_T = \sum_{j, \sigma} \tilde{t}_j c_{j, \sigma}^\dagger \sum_{\mathbf{k}} \Psi_{\mathbf{k}, \sigma}^\dagger e^{ik_x j} + h.c., \quad (4)$$

where the operator $c_{j, \sigma}^\dagger$ creates an electron of spin σ on site j . Since the total Hamiltonian is quadratic in the SC degrees of freedom, we can integrate them out, so that all the properties of the bulk superconductor and the tunneling to the nanowire are taken into account in the superconducting self-energy. The total Green's function of the system can be obtained by dressing the Green's function of the nanowire by the superconducting self-energy such that

$$\tilde{G}_R^{-1}(\omega) = \tilde{G}_{0R}^{-1}(\omega) - \tilde{\Sigma}_R^S(\omega). \quad (5)$$

The total retarded superconducting self-energy has the following form $\tilde{\Sigma}_R^S(\omega) = \mathcal{I} \otimes \tilde{\Sigma}_{j,R}^S(\omega)$, where \mathcal{I} is the unity matrix in the space of sites, and $\tilde{\Sigma}_{j,R}^S$ the on-site retarded self-energy

$$\tilde{\Sigma}_{j,R}^S(\omega) = |\tilde{t}_j|^2 \tau_z \tilde{g}_R(\omega) \tau_z, \quad (6)$$

$\tilde{g}_R(\omega)$ the Green's function of the superconductor. This Green's function is well known^{40,41} and can be incorporated using the superconducting self-energy

$$\hat{\Sigma}_{j,R}^S(\omega) = \Gamma_{j,S} \tilde{g}_R(\omega) = \Gamma_{j,S} \frac{\omega}{\sqrt{\Delta^2 - \omega^2}} \left(\mathbf{1} + \frac{\Delta}{\omega} \tau_x \right) \quad (7)$$

where $\mathbf{1}$ is the unity matrix in spin and particle-hole space, and $\Gamma_{j,S} = \pi \nu(0) |\tilde{t}_j|^2$ are the tunneling rates. The retarded bare Green's function of the semiconducting NW electrons is obtained by inverting the NW Hamiltonian

$$\tilde{G}_{0R}^{-1}(\omega) = (\omega + i\delta) \mathbf{1} - H_{NW} \quad (8)$$

where δ is an infinitesimal quasiparticle inverse lifetime introduced to avoid diverging terms in the numerical evaluations. This quantity determines the width of the bound states in the system.

We are interested in getting the local density of states evaluated at a given site j in the NW. Such a quantity can be obtained by taking the imaginary part of the total Green's function

$$LDOS = -\frac{1}{\pi} \sum_{\beta=\uparrow,\downarrow} \text{Im}[\tilde{G}_R^{jj,\beta\beta}(\omega)]. \quad (9)$$

The hopping amplitude is defined as $t = \hbar^2 / 2m^* a^2$ with $m^* = 0.0025m_e$ being the effective mass, a the lattice constant, and \hbar the Planck constant. The relation between the experimental and the tight binding parameters are determined by t . We use the maximum value of the gap $\Delta^* = 160 \mu\text{eV}$, in the short junction limit when it is fully formed, which corresponds to $t \approx 1.6 \text{meV}$ and a lattice constant of 70 nm. With these values, we can fully determine the parameters in the experiment. The only free parameters in our model is the lever arm which is taken to be 0.1 meV/mV similar as in the experiment (0.06 meV/mV). For the spin-orbit interaction strength we used 70 μeV , similar to what has been reported before.

Extracted QD and LS characteristics

Fig.S1a shows regular CB resonances over a large backgate voltage range in the normal state ($B = 50$ mT) at $V_{SD}=0$. A systematic increase of the resonance width is observed, with a strong variation between neighbouring charge states, possibly due to orbital effects. The average broadening Γ increases with increasing V_{BG} (see Fig.S1 b), consistent with an exponential increase with a linear reduction of the barrier height with respect to E_F .

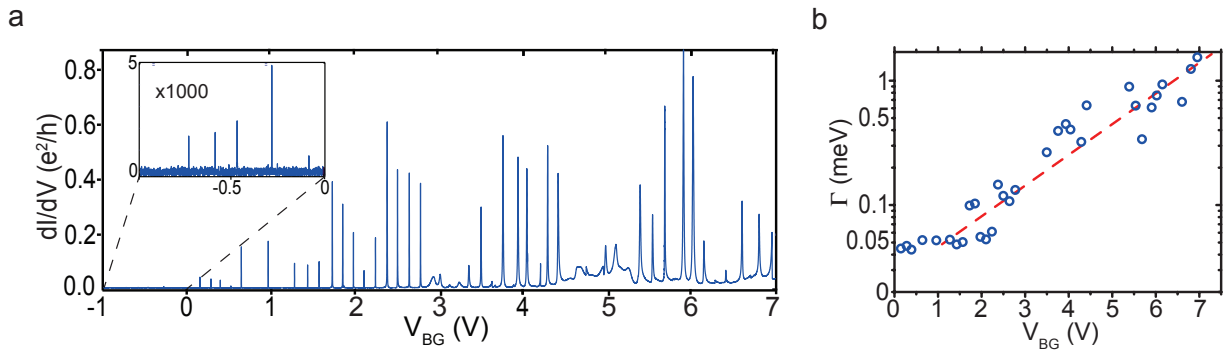


Figure S1: Gate voltage dependence of characteristic parameters. **a** Differential conductance as a function of V_{BG} . **b** Logarithmic plot of QD resonance width Γ (from Lorentzian fits) as a function of V_{BG} .

In Fig.S2a the schematic of the device structure is shown. The WZ tunnel barriers, defining the QD are represented in green. Fig.S2b shows the energy diagram of the conduction band edge E_{CB} relative to the Fermi energy E_F (dashed line) with an offset of ≈ 100 meV between WZ and ZB crystal phase.

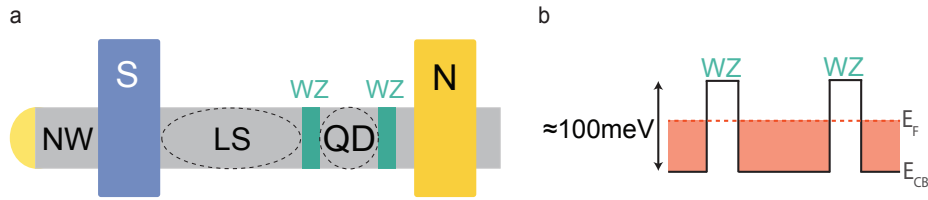


Figure S2: Schematic of the device structure and the band structure. **a** Schematic of the NW S-N device structure **b** Illustration of the energy diagram of the conduction band E_{CB} relative to the Fermi energy E_F .

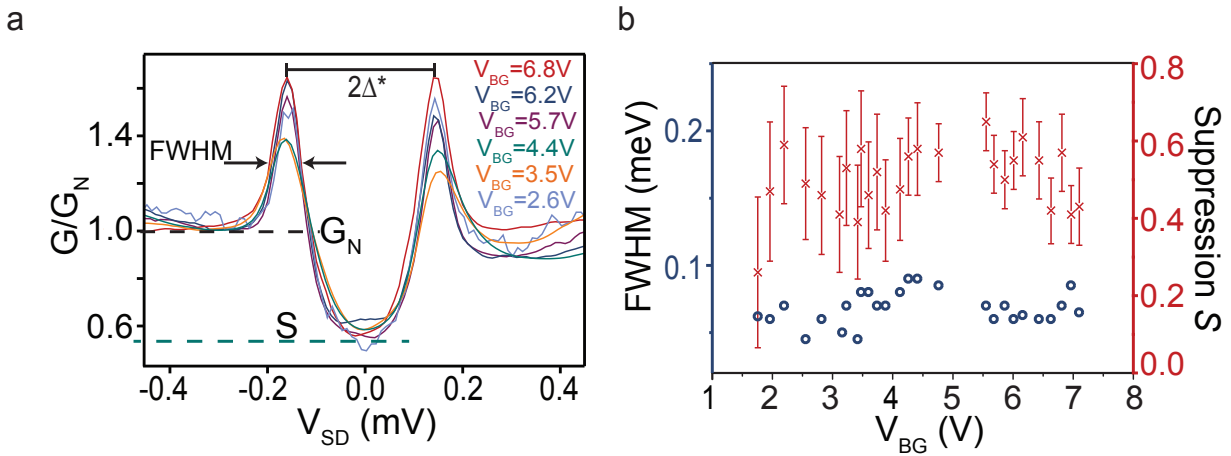


Figure S3: **a** Differential conductance G normalised to G_N as a function of V_{SD} at constant back-gate voltages in the cotunneling regime. **b** Full Width Half maximum (blue) of the coherence peaks and normalized zero bias suppression S (red) as a function V_{BG} .

Additional numerical calculations for an individual ABS

Fig.S4a shows the LDOS of an individual ABS as a function of the backgate voltage V_{BG} and source drain bias V_{SD} for a fixed junction length of $L = 350$ nm. Fig. S4b shows cross sections for the LDOS of an individual ABS for a fixed backgate voltage $V_{BG} = 0.4V$ and different lengths L .

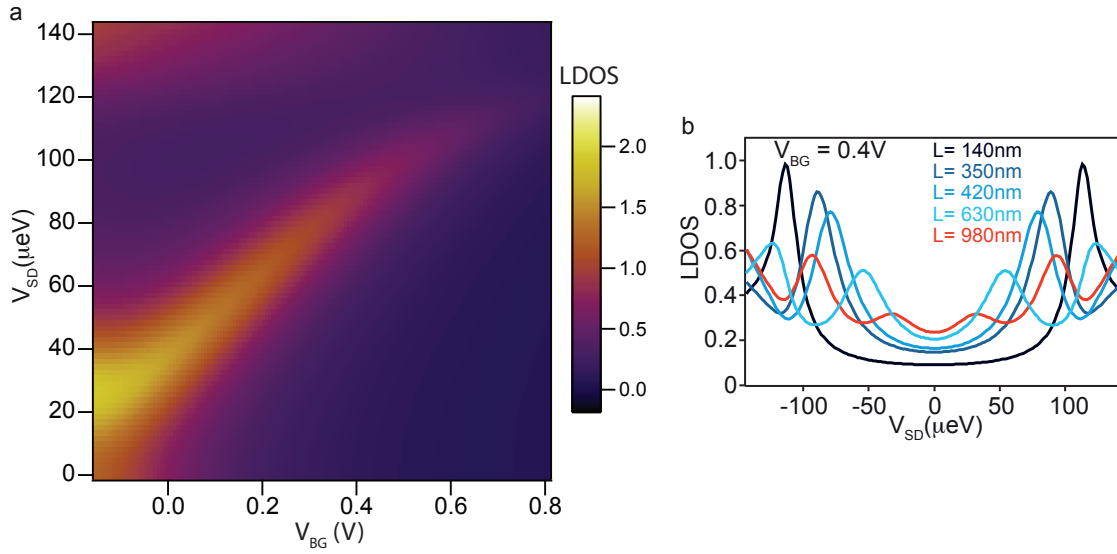


Figure S4: **a** Local density of states as a function of bias V_{SD} and backgate voltage V_{BG} at $L = 350$ nm. The ABSs width is set to $\Gamma_{ABS} = 25 \mu$ eV. **b** LDOS as a function of energy at various distances from the interface for a fixed gate voltage $V_{BG} = 0.4V$.

Additional measurements of S - I - S junction

Fig.S5 shows the normalized G of a S-I-S tunnel junction (consisting of Al-AlO₂-Al). The sample was measured in a similar measurement setup as the one discussed in the main text.

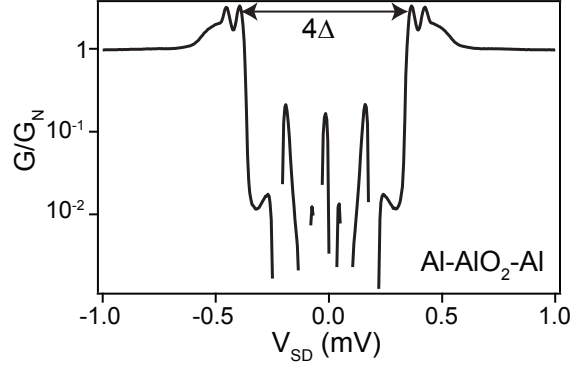


Figure S5: **a** Normalised conductance G/G_N as a function of V_{SD} of an S-I-S tunnel junction (made of Al- AlO₂-Al).

Additional numerical calculations for interface with disorder

Fig.S6 shows the LDOS as a function of the source drain bias V_{SD} (at $V_{BG} = 1$ V) at a distance of $L = 70$ nm from the S - N interface. The width of the ABS is set to $\Gamma_{ABS} = 4$ μ eV. The black cross section shows the LDOS without disorder at the interface. The red cross section shows the same cross section as before, but with a random potential fluctuation at the interface. This was realized by adding a random fluctuation (maximum +/- 130 μ eV) to the coupling of the superconductor ($\Gamma_{S,i} = 320$ μ eV) at each site i of the NW below. The randomized fluctuation value follows a

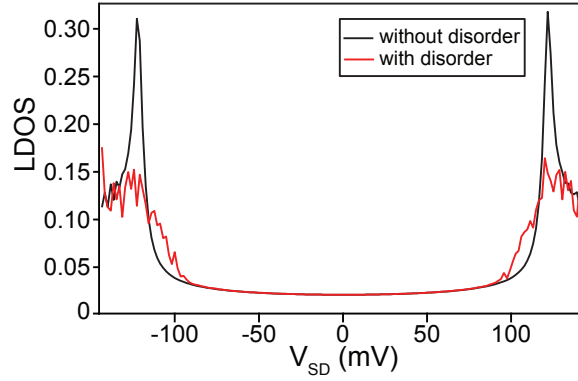


Figure S6: Local density of states as a function of bias V_{SD} without (black) and with (red) disorder.

The disorder LDOS was averaged 30 times.

Gaussian distribution. The plotted cross section was averaged 30 times. As a result, the peaks at the gap edge are smaller in amplitude and also broadened, compared to the clean case. The edges of the gap appear to be slightly smoother.

References

1. Beenakker, C. W. J. Quantum transport in semiconductor-superconductor microjunctions. *Physical Review B* **46**, 12841–12844 (1992).
2. Hofstetter, L., Csonka, S., Nygård, J. & Schönberger, C. Cooper pair splitter realized in a two-quantum-dot y-junction. *Nature* **461**, 960–963 (2009).
3. Schindele, J., Baumgartner, A. & Schönberger, C. Near-unity cooper pair splitting efficiency. *Physical Review Letters* **109** (2012).
4. Cleuziou, J.-P., Wernsdorfer, W., Bouchiat, V., Ondaçuhu, T. & Monthieux, M. Carbon nanotube superconducting quantum interference device. *Nature Nanotechnology* **1**, 53–59 (2006).
5. Mourik, V. *et al.* Signatures of majorana fermions in hybrid superconductor-semiconductor nanowire devices. *Science* **336**, 1003–1007 (2012).
6. Albrecht, S. M. *et al.* Exponential protection of zero modes in majorana islands. *Nature* **531**, 206–209 (2016).
7. Deng, M. T. *et al.* Majorana bound state in a coupled quantum-dot hybrid-nanowire system. *Science* **354**, 1557–1562 (2016).
8. Zhang, H. *et al.* Quantized majorana conductance. *Nature* **556**, 74–79 (2018).

9. Alicea, J., Oreg, Y., Refael, G., von Oppen, F. & Fisher, M. P. A. Non-abelian statistics and topological quantum information processing in 1d wire networks. *Nature Physics* **7**, 412–417 (2011).
10. Nayak, C., Simon, S. H., Stern, A., Freedman, M. & Sarma, S. D. Non-abelian anyons and topological quantum computation. *Reviews of Modern Physics* **80**, 1083–1159 (2008).
11. Leijnse, M. & Flensberg, K. Scheme to measure majorana fermion lifetimes using a quantum dot. *Physical Review B* **84** (2011).
12. Hoffman, S., Chevallier, D., Loss, D. & Klinovaja, J. Spin-dependent coupling between quantum dots and topological quantum wires. *Physical Review B* **96** (2017).
13. Chevallier, D., Szumniak, P., Hoffman, S., Loss, D. & Klinovaja, J. Topological phase detection in rashba nanowires with a quantum dot. *Physical Review B* **97** (2018).
14. Gharavi, K., Hoving, D. & Baugh, J. Readout of majorana parity states using a quantum dot. *Physical Review B* **94** (2016).
15. Dick, K. A., Thelander, C., Samuelson, L. & Caroff, P. Crystal phase engineering in single InAs nanowires. *Nano Letters* **10**, 3494–3499 (2010).
16. Lehmann, S., Wallentin, J., Jacobsson, D., Deppert, K. & Dick, K. A. A general approach for sharp crystal phase switching in InAs, GaAs, InP, and GaP nanowires using only group v flow. *Nano Letters* **13**, 4099–4105 (2013).

17. Rossella, F. *et al.* Nanoscale spin rectifiers controlled by the stark effect. *Nature Nanotechnology* **9**, 997–1001 (2014).
18. Nilsson, M. *et al.* Tuning the two-electron hybridization and spin states in parallel-coupled InAs quantum dots. *Physical Review Letters* **121** (2018).
19. Nilsson, M. *et al.* Single-electron transport in InAs nanowire quantum dots formed by crystal phase engineering. *Physical Review B* **93** (2016).
20. Chen, I.-J. *et al.* Conduction band offset and polarization effects in InAs nanowire polytype junctions. *Nano Letters* **17**, 902–908 (2017).
21. Doh, Y.-J., Franceschi, S. D., Bakkers, E. P. A. M. & Kouwenhoven, L. P. Andreev reflection versus coulomb blockade in hybrid semiconductor nanowire devices. *Nano Letters* **8**, 4098–4102 (2008).
22. Gramich, J., Baumgartner, A. & Schönenberger, C. Resonant and inelastic andreev tunneling observed on a carbon nanotube quantum dot. *Physical Review Letters* **115** (2015).
23. Gramich, J., Baumgartner, A. & Schönenberger, C. Andreev bound states probed in three-terminal quantum dots. *Physical Review B* **96** (2017).
24. Court, N. A., Ferguson, A. J. & Clark, R. G. Energy gap measurement of nanostructured aluminium thin films for single cooper-pair devices. *Superconductor Science and Technology* **21**, 015013 (2007).

25. Franceschi, S. D. *et al.* Electron cotunneling in a semiconductor quantum dot. *Physical Review Letters* **86**, 878–881 (2001).
26. Doh, Y.-J. Tunable supercurrent through semiconductor nanowires. *Science* **309**, 272–275 (2005).
27. Sand-Jespersen, T. *et al.* Kondo-enhanced andreev tunneling in InAs nanowire quantum dots. *Physical Review Letters* **99** (2007).
28. Jellinggaard, A., Grove-Rasmussen, K., Madsen, M. H. & Nygård, J. Tuning yu-shiba-rusinov states in a quantum dot. *Physical Review B* **94** (2016).
29. Gramich, J., Baumgartner, A. & Schönenberger, C. Subgap resonant quasiparticle transport in normal-superconductor quantum dot devices. *Applied Physics Letters* **108**, 172604 (2016).
30. Yeyati, A. L., Cuevas, J. C., López-Dávalos, A. & Martín-Rodero, A. Resonant tunneling through a small quantum dot coupled to superconducting leads. *Physical Review B* **55**, R6137–R6140 (1997).
31. Dynes, R. C., Narayanamurti, V. & Garno, J. P. Direct measurement of quasiparticle-lifetime broadening in a strong-coupled superconductor. *Physical Review Letters* **41**, 1509–1512 (1978).
32. Bagwell, P. F. Suppression of the josephson current through a narrow, mesoscopic, semiconductor channel by a single impurity. *Physical Review B* **46**, 12573–12586 (1992).

33. Bena, C. Metamorphosis and taxonomy of andreev bound states. *The European Physical Journal B* **85** (2012).
34. Krogstrup, P. *et al.* Epitaxy of semiconductor–superconductor nanowires. *Nature Materials* **14**, 400–406 (2015).
35. Chang, W. *et al.* Hard gap in epitaxial semiconductor–superconductor nanowires. *Nature Nanotechnology* **10**, 232–236 (2015).
36. Takei, S., Fregoso, B. M., Hui, H.-Y., Lobos, A. M. & Sarma, S. D. Soft superconducting gap in semiconductor majorana nanowires. *Physical Review Letters* **110** (2013).
37. Liu, C.-X., Setiawan, F., Sau, J. D. & Sarma, S. D. Phenomenology of the soft gap, zero-bias peak, and zero-mode splitting in ideal majorana nanowires. *Physical Review B* **96** (2017).
38. Liu, C.-X., Sau, J. D., Stanescu, T. D. & Sarma, S. D. Andreev bound states versus majorana bound states in quantum dot-nanowire-superconductor hybrid structures: Trivial versus topological zero-bias conductance peaks. *Physical Review B* **96** (2017).
39. Reeg, C., Dmytruk, O., Chevallier, D., Loss, D. & Klinovaja, J. Zero-energy andreev bound states from quantum dots in proximitized rashba nanowires. *Physical Review B* **98**, 245407 (2018).
40. Cuevas, J. C., Martín-Rodero, A. & Yeyati, A. L. Hamiltonian approach to the transport properties of superconducting quantum point contacts. *Physical Review B* **54**, 7366–7379 (1996).

41. Chevallier, D., Rech, J., Jonckheere, T. & Martin, T. Current and noise correlations in a double-dot cooper-pair beam splitter. *Physical Review B* **83** (2011).